

<https://doi.org/10.1038/s44306-024-00055-y>

Absence of magnetic order in RuO₂: insights from μ SR spectroscopy and neutron diffraction

Check for updates

Philipp Keßler^{1,2,7}, Laura Garcia-Gassull^{3,7}, Andreas Suter⁴, Thomas Prokscha⁴, Zaher Salman⁴✉, Dmitry Khalyavin⁵, Pascal Manuel⁵✉, Fabio Orlandi⁵, Igor I. Mazin⁶✉, Roser Valenti³✉ & Simon Moser^{1,2}✉

Altermagnets are a novel class of magnetic materials, where magnetic order is staggered both in coordinate and momentum space. The metallic rutile oxide RuO₂, long believed to be a textbook Pauli paramagnet, recently emerged as a putative workhorse altermagnet when resonant X-ray and neutron scattering studies reported nonzero magnetic moments and long-range collinear order. While some experiments seem consistent with altermagnetism, magnetic order in RuO₂ remains controversial. We show that RuO₂ is nonmagnetic, both in bulk and thin film. Muon spectroscopy complemented by density-functional theory finds at most $1.14 \times 10^{-4} \mu_B/\text{Ru}$ in bulk and at most $7.5 \times 10^{-4} \mu_B/\text{Ru}$ in 11 nm epitaxial films, at our spectrometers' detection limit, and dramatically smaller than previously reported neutron results that were used to rationalize altermagnetic behavior. Our own neutron diffraction measurements on RuO₂ single crystals identify multiple scattering as the source for the false signal in earlier studies.

Altermagnetism, a magnetic state of matter that shares properties with both conventional ferro- and antiferromagnets^{1,2}, has recently garnered considerable attention. While altermagnets exhibit the typical ferromagnetic signature of spin split energy bands, they still retain the zero net magnetization that is characteristic of an antiferromagnet³. Since one of the first articles on the subject⁴, a number of theoretical and experimental studies aimed at exploring fingerprints of altermagnetism have been conducted^{5–13}, but a definitive reproducible experimental detection of the altermagnetic state remains elusive. A plurality of experiments, in particular, have been performed on the metallic rutile oxide RuO₂^{6,8,13–19}, where both resonant X-ray scattering²⁰ and neutron diffraction experiments²¹ reported a $\mathbf{q} = \mathbf{0}$ antiferromagnetic pattern that is consistent with altermagnetic symmetry constraints. Nonetheless, in the earlier neutron report²¹, two caveats were noted: firstly, polarized neutron diffraction refinement resulted in an ordered moment of approximately $\sim 0.05 \mu_B/\text{Ru}$. This value is at least one order of magnitude smaller than the numbers used to interpret subsequent experiments^{6,8}, but still two orders of

magnitude larger than what was found recently by the muon spin relaxation/rotation (μ SR) technique on RuO₂ single crystals¹⁸.

Secondly, electronic structure calculations in the framework of density functional theory (DFT) converge, without additional nudging, to a nonmagnetic solution^{15,21,22}. Only the addition of a sizable Hubbard U – somewhat uncommon for good 4d metals – can generate ordered magnetic moments. In this context, it has been suggested that the presence of Ru vacancies may lead to magnetism at a lower and more realistic Hubbard U ²² than that used in refs. 4,23.

In view of the popularity and conceptual importance of RuO₂ as a prototypical altermagnet, it is essential to verify the existence and strength of the magnetic order in this compound. We thus have revisited the question about ordered moments in RuO₂ and performed careful neutron diffraction experiments employing state-of-the-art time-of-flight detection. Surprisingly, we found that the previously reported and alleged magnetic (1,0,0) reflection²¹ is likely related to a multiple scattering artifact rather than to a magnetic origin. Further, we employed the highly sensitive μ SR technique, complemented by DFT calculations of the muon stopping sites and

¹Physikalisches Institut, Universität Würzburg, 97074 Würzburg, Germany. ²Würzburg–Dresden Cluster of Excellence ct.qmat, Universität Würzburg, 97074 Würzburg, Germany. ³Institut für Theoretische Physik, Goethe-Universität, 60438 Frankfurt am Main, Germany. ⁴Laboratory for Muon Spin Spectroscopy, Paul Scherrer Institute, CH-5232 Villigen PSI, Switzerland. ⁵ISIS Pulsed Neutron and Muon Source, STFC Rutherford Appleton Laboratory, Didcot, OX11 0QX, United Kingdom. ⁶Department of Physics & Astronomy and Quantum Science and Engineering Center, George Mason University, Fairfax, VA, USA. ⁷These authors contributed equally: Philipp Keßler, Laura Garcia-Gassull. ✉e-mail: zaher.salman@psi.ch; pascal.manuel@stfc.ac.uk; imazin2@gmu.edu; valenti@itp.uni-frankfurt.de; simon.moser@uni-wuerzburg.de

hyperfine fields, and determined an upper bound on magnetic moments of $1.14 \times 10^{-4} \mu_B/\text{Ru}$ in the bulk and $7.5 \times 10^{-4} \mu_B/\text{Ru}$ in 11 nm epitaxial thin films of RuO_2 , consistent with a recent bulk value obtained by an independent group¹⁸.

These moments are two orders of magnitude smaller than what was reported by the previous neutron study²¹, and essentially reflect the detection limit of the utilized spectrometer. Hyperfine field calculations in stoichiometric and Ru vacant RuO_2 further exclude any fortuitous cancellation of hyperfine fields at the muon stopping site. We thus conclude that RuO_2 exhibits no long-range magnetic order, neither in the bulk nor in epitaxial thin films, and the altermagnetic signatures reported in multiple earlier publications^{6,8,11,13,16,17} likely have extrinsic origin.

Experimental results

RuO₂ samples

To shed light on the magnetic properties of RuO_2 , we investigated three different types of samples: (i) Millimeter sized RuO_2 crystals that were grown by chemical vapor transport at the Crystal Growth Facility of the EPFL in Lausanne, Switzerland, following a recipe described in refs. 24,25; (ii) 11 nm thick RuO_2 epitaxial thin films grown on $\text{TiO}_2(110)$ by pulsed laser deposition at the Institute of Physics, Würzburg, Germany, following our recipe developed in refs. 8,26; and (iii) 99.9% pure (trace metals basis) RuO_2 powder purchased from Sigma-Aldrich that was measured without further preparation steps. The structural and stoichiometric integrity of all three RuO_2 samples was verified by x-ray diffraction and x-ray photoelectron spectroscopy (see Supplementary Information).

Neutron diffraction results

Reassessing the results of the earlier study²¹, we first performed single crystal neutron diffraction on the RuO_2 crystals. As discussed above, altermagnetism in RuO_2 implies a $\mathbf{q} = \mathbf{0}$ propagation vector and antiparallel magnetic coupling of the two Ru sites in the primitive unit cell, with moments polarized along the crystal c -axis. The structure is expected to result in a strong magnetic scattering to the structurally forbidden $(1, 0, 0)$ reflection²¹. This is due to the fact that the two magnetic sites are summed over in the corresponding structure factor and the moments are perpendicular to the scattering vector.

In addition, among all possible magnetic reflections with $\mathbf{q} = \mathbf{0}$, the $(1, 0, 0)$ one has the largest d -spacing and therefore the largest value of the magnetic form factor. A model of lower symmetry, where the Neel vector departs from the c -axis, has been discussed in ref. 27. Despite of the general direction of the magnetic dipoles, the model still predicts the $(1, 0, 0)$ to be the strongest magnetic reflection. We thus focused our attention at the $(1, 0, 0)$ reflection and measured it at different scattering angles 2θ , thereby using different neutron wavelengths λ , and found a strong dependence on the scattering geometry. At some scattering angles, the reflection was not observed even after ten hours of statistics, in spite of a good optimization with respect of the neutron flux, whereas at some other angles (mainly low angles) it was detectable within a few minutes with a poorer flux optimization (Fig. 1). This behavior is not typical for a real Bragg peak and is known as Renninger effect^{28–30}, caused by multiple scattering processes (often referred to as double scattering).

This can happen when two reciprocal lattice nodes, \mathbf{K}_1 and \mathbf{K}_2 , are present simultaneously on the surface of the Ewald sphere. Let us denote the Miller indices of the corresponding families of lattice planes as (h_1, k_1, l_1) and (h_2, k_2, l_2) , then the corresponding Laue conditions are: $(\mathbf{k}_1 - \mathbf{k}_0)/\lambda = \mathbf{K}_1$ and $(\mathbf{k}_2 - \mathbf{k}_0)/\lambda = \mathbf{K}_2$, where \mathbf{k}_0 is the unit vector along the incident beam and \mathbf{k}_1 , \mathbf{k}_2 are directions of the diffracted beam. By subtracting the second equation from the first, one obtains $(\mathbf{k}_1 - \mathbf{k}_2)/\lambda = \mathbf{K}_1 - \mathbf{K}_2$. This indicates that the beam diffracted by the (h_1, k_1, l_1) in the direction \mathbf{k}_1 overlaps with a double-scattering beam, first by the plane (h_2, k_2, l_2) in the direction \mathbf{k}_2 and then by the plane $(h_1 - h_2, k_1 - k_2, l_1 - l_2)$ in the direction \mathbf{k}_1 (see inset of Fig. 1(b) for an illustration). If (h_1, k_1, l_1) is a systematically absent structural reflection, then the Renninger effect may result in an apparent violation of the reflection conditions³¹ or can be interpreted as magnetic scattering.

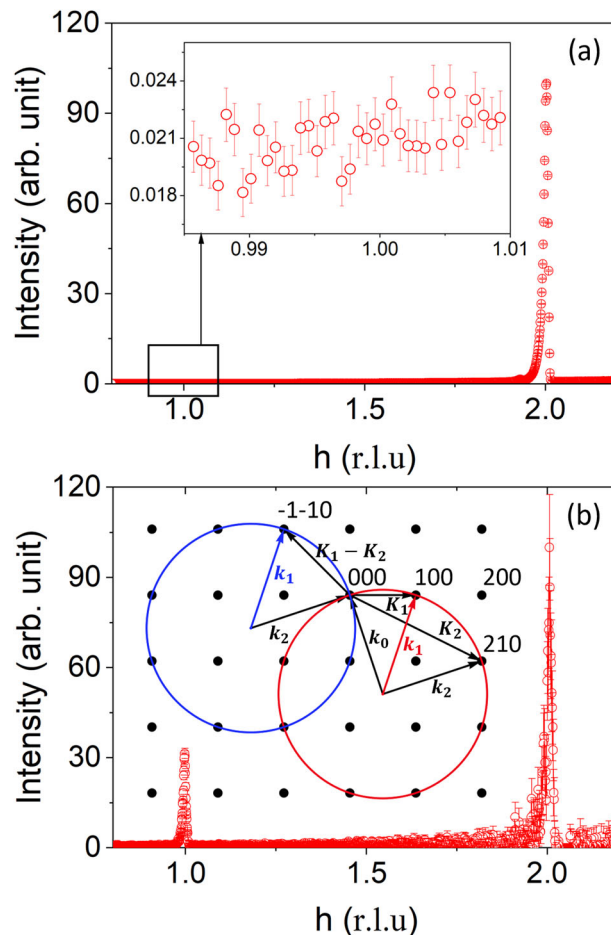


Fig. 1 | Neutron diffraction of a RuO_2 single crystal. The data was collected at $T = 1.5 \text{ K}$ with the $(h, 0, 0)$ reflections at the scattering angle $2\theta = 71^\circ$ (a) and $2\theta = 32^\circ$ (b). The counting time was 10 hours and 15 minutes, respectively. The data demonstrate 1D cuts of the reciprocal lattice along the $(h, 0, 0)$ direction. The inset of (b) shows a simple two-dimensional illustration of the double diffraction, taking place when the Ewald sphere intersects both the $\mathbf{K}_1 = (1, 0, 0)$ and $\mathbf{K}_2 = (2, 1, 0)$ reciprocal lattice points. The beam, first scattered by the $(2, 1, 0)$ planes in the direction \mathbf{k}_2 , is then scattered again by the $(-1, -1, 0)$ planes in the direction \mathbf{k}_1 , where the $(1, 0, 0)$ scattering is expected. The intersection of the $(h, k, 0)$ reciprocal plane and the Ewald sphere is shown by the red circle for the first scattering process (from the $(2, 1, 0)$ planes) and by the blue circle for the second scattering process (by the $(-1, -1, 0)$ planes).

As the radius of the Ewald sphere is defined by the wavelength λ of the incident and scattered neutrons, the double scattering process is expected to be strongly λ -dependent and should not take place if the necessary conditions are not satisfied. Observation of the doubly scattered beam will thus only exist in a finite angular range due to beam divergence and finite extension of the Bragg spots in reciprocal space, controlled by sample quality and instrument resolution. At low scattering angles, where the Bragg law selects short wavelengths, the radius of the Ewald sphere is big, and the sphere has a large surface in reciprocal space. Further, instrumental resolution also quickly degrades with decreasing scattering angles. This strongly increases the probability that two (or more) reciprocal spots hit the sphere producing the multiple scattering. Consequently, the Renninger effect is the most natural explanation for the presence of the $(1, 0, 0)$ reflection in RuO_2 and its strong dependence on the scattering angle (or equivalently the wavelength of neutrons). In the context of the present study, the key experimental observation is the lack of the $(1, 0, 0)$ reflection in the well-optimized (in respect of the neutron flux) scattering geometry. After ten hours of measurements, the statistic of the data allows us to rule out the $\mathbf{q} = \mathbf{0}$

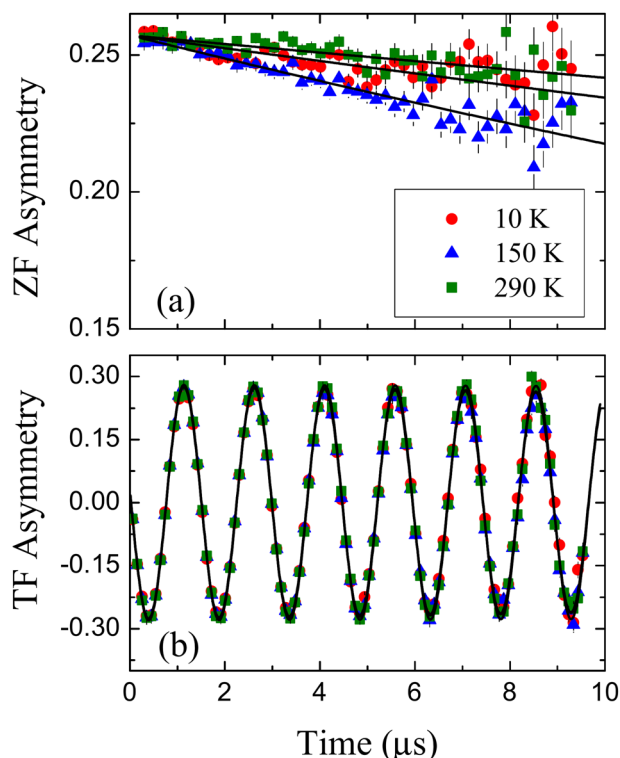


Fig. 2 | Muon spin relaxation/rotation asymmetry of bulk RuO₂. Representative curves were measured for (a) zero and (b) weak transverse magnetic field at various temperatures.

magnetic ordering with moment size bigger than $0.011 \mu_B$, a value at least five times smaller than that previously proposed in ref. 21. Moreover, we explored a large portion of the reciprocal space available in the time-of-flight scattering experiment and have not found any evidence of magnetic ordering neither with $q = 0$ nor with some other propagation vector. This strongly supports the non-magnetic nature of the RuO₂ crystals.

Muon spin relaxation/rotation (μ SR) results

For further insights on their size, we employed the μ SR technique as a highly sensitive probe of static local magnetic moments. In a μ SR measurement, fully polarized muons are implanted into the sample. Muons decay with a lifetime of $2.2 \mu\text{s}$, emitting a positron preferentially in the direction of the spin polarization at the time of decay. The spatial distribution of these positrons is monitored as a function of time using plastic scintillating detectors placed around the studied sample. Therefore, the asymmetry in the decay of positrons on opposite sides of the sample, $A(t)$, is proportional to the polarization along the corresponding axis. In practice, $A(t)$ is calculated via

$$A(t) = \frac{N_U - \alpha_{UD}N_D}{N_U + \alpha_{UD}N_D}, \quad (1)$$

where N_U and N_D are the number of positrons detected as a function of time in detectors placed above (U) and below (D) the sample, respectively. α_{UD} is a geometric correction factor to account for the different efficiencies of the U and D detectors.

In the bulk μ SR measurements (GPS), we performed primarily measurements on the powder sample in zero applied external field (ZF) and in weak transverse field (TF - transverse to the initial muon spin polarization). A few measurements obtained from the single crystal gave results that are – within error – equal to the powder measurements. Therefore, we hereafter focus only on the powder measurements. In Fig. 2(a), we show typical asymmetry curves measured at three different temperatures.

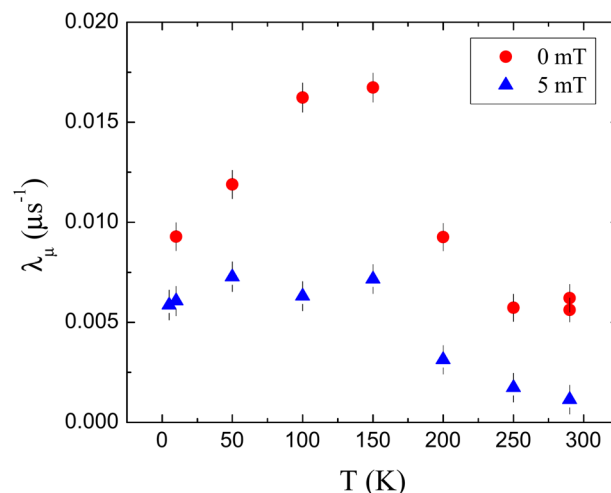


Fig. 3 | Muon spin relaxation rate in bulk RuO₂. The temperature dependence was extracted from measurements in zero-field and transverse-field geometries.

We observe no significant relaxation or depolarization at any temperature and no missing asymmetry, confirming that the local magnetic fields sensed by the implanted muons are extremely small, comparable to other non-magnetic materials such as gold and silver. Only a slight increase in the relaxation rate around ~ 150 K is observed. Similar results were obtained from μ SR measurements while applying a TF of 5 mT. A few representative asymmetry spectra are depicted in Fig. 2b. The applied field in this case leads to a Larmor precession of the muons' spin polarization, and therefore, an oscillation in the asymmetry spectra. In the case of a strongly magnetic sample with large internal magnetic fields (larger than the applied field), the initial amplitude of these oscillations is proportional to the paramagnetic volume fraction of the sample. However, if the internal magnetic fields are much smaller than the applied field, then the damping rate of the oscillations increases below the magnetic transition temperature. Just as in the case of the ZF measurements, no significant temperature dependence in the amplitude and damping rate was observed in the TF measurements, ruling out any static magnetic order in RuO₂ (neither short nor long range).

To analyse the data, we fit the asymmetries using an exponentially damped oscillation, $A(t) = A_0 \exp(-\lambda_\mu t) \cos(\omega t + \varphi)$. Both ZF and TF data were fitted using a temperature independent initial asymmetry A_0 and phase φ , while the relaxation rate λ_μ and frequency ω were temperature dependent. For the ZF measurements, we use $\omega = 0$ and $\varphi = 0$. The relaxation rates obtained from these fits are shown in Fig. 3.

We note a very small temperature dependence in λ_μ measured in both ZF and TF. In particular, in the ZF measurements we observe a peak around ~ 150 K, which corresponds to the small enhancement in relaxation seen in the raw spectra of Fig. 2a. The origin of this peak is not fully understood, but may be related to the muon's spin lattice relaxation. In contrast, in the TF measurements, λ_μ increases slightly below ~ 200 K but saturates below ~ 150 K. This small temperature dependence and extremely small relaxation rate, however, cannot be attributed to static magnetic order in RuO₂, which would generally result in much larger values of λ_μ . We note that our results are somewhat different from those presented in ref. 18. We attribute this to differences in fitting function (exponential vs. Gaussian) and fitting procedure (temperature independent vs. temperature dependent initial asymmetry).

In order to probe a possible magnetic order (or static magnetic moments) near grain boundaries, interface, or other defects, we performed low energy μ SR (LE- μ SR) measurements on 11 nm thick epitaxial RuO₂(110) films deposited on top of a TiO₂ rutile substrate. In the LE- μ SR, the implantation energy of the muons, E_i was varied between 1 keV and 12 keV, resulting in an implantation depth (probing depth) between ~ 5 nm and ~ 100 nm (see Fig. 4). Typical LE- μ SR asymmetry curves measured at three

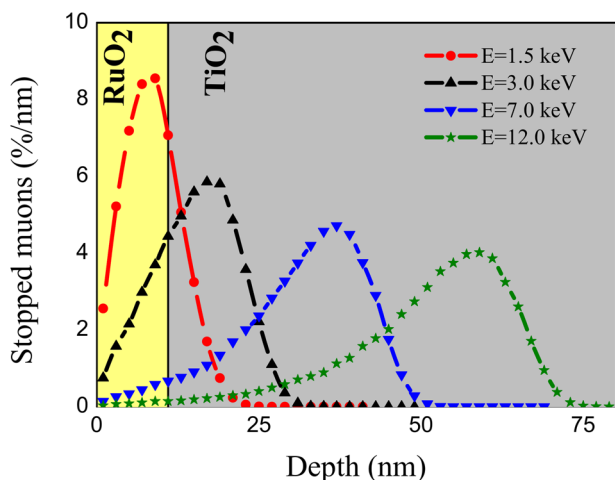


Fig. 4 | Muon stopping depth profiles. Muon stopping profiles calculated as a function of depth for the different implantation energies in an 11 nm thick RuO₂ film on a TiO₂ substrate.

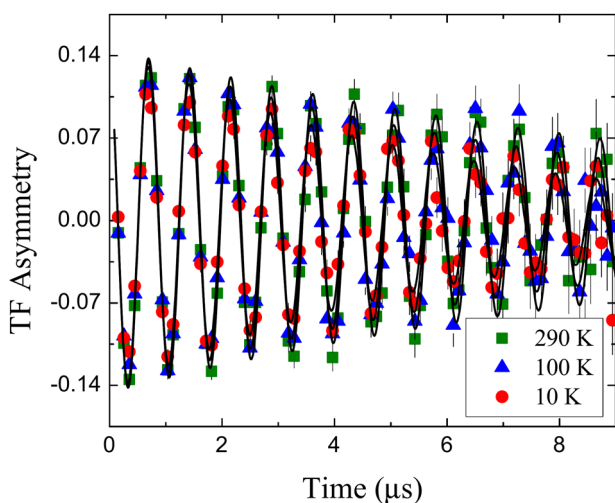


Fig. 5 | Muon spin rotation asymmetry of 11 nm thick RuO₂ films. Representative curves were measured with 10 mT transverse magnetic field and $E = 1.5$ keV at various temperatures.

different temperatures are shown in Fig. 5. The resulting damping rate, λ_μ , is plotted as a function of temperature for both implantation energies in Fig. 6 as a function of temperature for $E = 1.5$ keV and $E = 12$ keV, corresponding to muons stopping primarily in the RuO₂ layer and the substrate, respectively.

We find that λ_μ in the RuO₂ layer, though generally higher than what we found in the bulk, remains quite small. This rules out the presence of large magnetic fields in these films. We also note that λ_μ in RuO₂ is much larger than that measured in the TiO₂ substrate. Therefore, the enhanced relaxation rate in the RuO₂ layer cannot be attributed to the fraction of muons stopping in the substrate. Moreover, the gradual increase in λ_μ with decreasing temperature rules out background contribution due to back-scattered muons³². Instead, we believe that the observed increase in relaxation compared to the bulk is due to the presence of somewhat larger magnetic moments in films of RuO₂. The origin of these magnetic moments may be defects or vacancies³³, or epitaxial strain (see Supplementary Information), which might be more abundant in the films. Note that the equal relaxation rates measured in bulk crystals and powder points to the fact that (i) the density of vacancies and defects are similar in both and (ii) the size of their associated magnetic moments are very small.

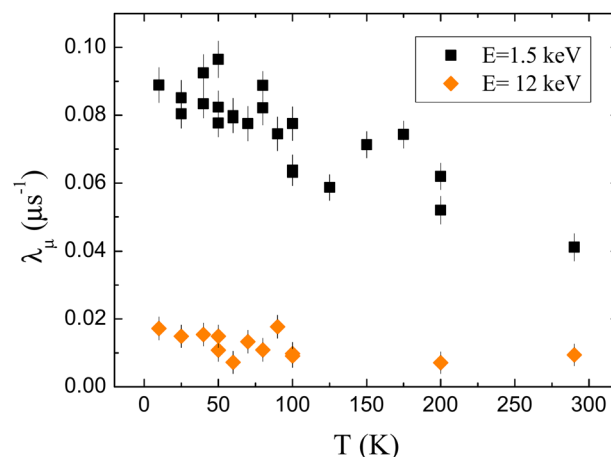


Fig. 6 | Muon spin relaxation rate in 11 nm thick RuO₂ films. The temperature dependence was extracted from measurements in 10 mT transverse-field. At $E = 1.5$ keV most of the muons stop in the RuO₂ layer while at $E = 12$ keV they stop in the substrate.

Discussion

In order to better interpret the results of the μ SR measurements, we performed first-principles calculations based on spin-polarized density functional theory (DFT), and enforcing a magnetic moment on the Ru atoms by adding a large effective Hubbard U^{22} , as also done in other computational studies^{4,23}. To emulate the muon stopping site, we used the standard protocol described in ref. 34. As muon and proton are identical from the point of view of adiabatic DFT calculations, we used a proton in place of the muon, thinking of the muon as a light proton³⁵. The total number of electrons was kept unchanged. This proton was implanted into a sufficiently large ($3 \times 3 \times 3$) supercell to avoid interaction with its replicas in the neighboring cells³⁴.

RuO₂ crystallizes in the rutile structure, space group $P4_2/mnm$, as depicted in supplementary Fig. S4. This structure, which we here call “pristine”, serves as the basis for DFT calculations involving a muon. The calculated magnetic moment on the Ru atoms, for $U_{eff} = 1.4$ eV, was $0.866 \mu_B/\text{Ru}$. This magnetic moment was used in the interpretation of the experiments done in refs. 5,6,8,11,13,20,21,36. In addition to the pristine structure, we emulated the effect of potential Ru vacancies by removing one Ru from this supercell (i.e., 1.8% of Ru vacancies as reported in at least one case³⁷), which enhances the tendency to magnetism²². We also checked the stability of the results against adding spin-orbit coupling (SOC), and found that both in the pristine case and in the presence of a Ru vacancy, SOC introduces negligible effects, in agreement with the previous literature^{23,25}. To optimize computing time we thus performed our calculations without SOC.

First, we identified probable stopping sites for a muon by looking at the electrostatic potential in the pristine unit cell, as shown in Fig. 7. This electrostatic potential is defined as the sum of the ionic potential and the Hartree potential.

As Fig. 7 shows, and Fig. 8 further highlights, the electrostatic potential suggests the presence of channels along the crystal c direction, where we expect the muon to be initially attracted to. Within a channel, the electrostatic potential minima are the points farthest away from the Ru ions. They are indicated in Fig. 8 by little orange balls.

Taking a closer look at Fig. 8, and focusing on one color, i.e., one value of the electrostatic potential, we can construct an equipotential surface that is oriented along the c axis (see supplementary Fig. S4 for an example). The tube-like shape indicates the above-mentioned channel to which a muon will be immediately attracted. Full optimization of the muon, Ru and O positions further shows that the muons displace away from the axis of the tube to form a bond with one of the nearby oxygens (see Fig. 9), as is typical in ionic crystals³⁴. Although along the c -axis the radii of the tubes diminish in the region between two Ru layers, there is a possibility of a thermally-activated muon diffusion

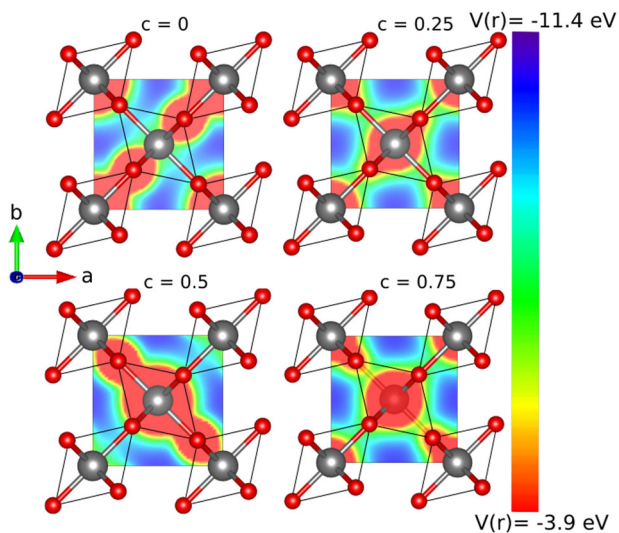


Fig. 7 | Crystal structure and electrostatic potential maps for different cuts along c in units of the lattice parameter. The electrostatic potential is represented by the color map from red to blue. The purple shade indicates regions where the (negative) electrostatic potential is the largest, i.e., the likely muon stopping sites. The color map is limited to the unit cell.

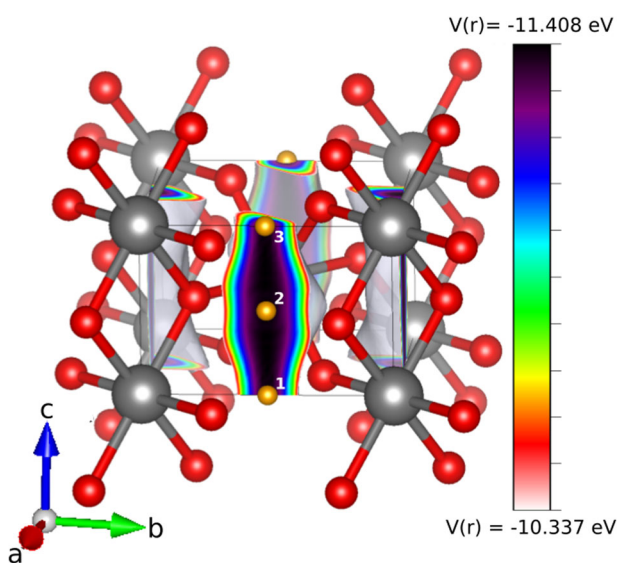


Fig. 8 | Initial approximation of the stopping sites of the muon, represented by orange balls, where the electrostatic potential is highest. The color map indicates that, the maxima of the potential occurs at the furthest distance from Ru atoms. These positions are the most likely stopping sites along the channel, as seen in the minima of the energy in Fig. 10.

along these channels, which can affect the muon depolarization by averaging the local magnetic fields. In order to check this, we performed constrained optimization, fixing the z coordinate of the muon and relaxing all other internal parameters. Since this is a rather time-consuming procedure, we performed all calculations on an $2 \times 2 \times 4$ k -mesh, starting from a low k -mesh density and increasing it as the calculations converged. The result is shown in Fig. 10. We find the minima labeled 1–3 in Fig. 8 to be at least 600 meV deep. This barrier height ensures that muons do not diffuse between these stopping sites under our experimental conditions.

Beyond the pristine system, long range static magnetic order in RuO_2 was suggested to be induced by hole doping due to Ru vacancies²². To account for this possibility, we conducted two sets of calculations: with and

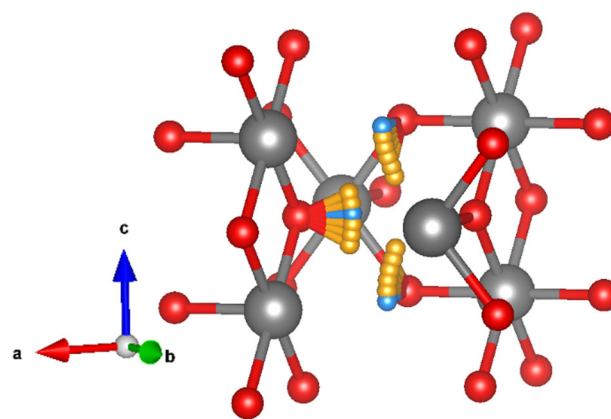


Fig. 9 | Final stopping sites of the muon (represented in orange or blue) for different positions along the c axis. In blue, we specify those positions with the lowest energy, i.e. the most likely stopping sites.

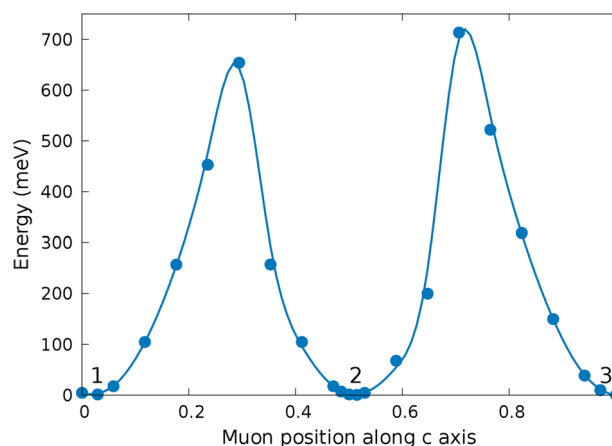


Fig. 10 | Energy calculated for a diffusion path of a muon along the c direction from one Ru spin-equivalent plane to the next, in fractional coordinates with $U_{eff} = 1.4$ eV. The muon’s position along a and b was relaxed. The most likely stopping sites are in the planes of the Ru atoms, as labeled in Fig. 8. The line is a guide to the eye. Please note that the energy landscape should be periodic, and the observed deviations on the order of ± 50 meV serve as an independent gauge of reliability of our calculations.

without a Ru vacancy in the $3 \times 3 \times 3$ supercell. In the former case, we considered both the same stopping site as in a pristine crystal, again with full re-optimization, and a second case where the muon was put near a vacancy, followed by additional atomic relaxation (see Supplementary Information). As seen in supplementary Fig. S6, the electrostatic potential increases at the Ru vacancy (in absolute values). When placing a muon nearby the vacancy, however, it converged to a position further away from the Ru atoms than in the pristine case, revealing no new energetically favorable stopping sites.

The hyperfine field acting on the muon was calculated for both the structures with and without Ru vacancies. For different U_{eff} in the pristine case, the values of the hyperfine field and the magnetic moment of the Ru atoms are shown in Fig. 11. As expected in a good metal, we find that the hyperfine field is dominated by the Fermi-contact term due to the finite polarization of the electronic cloud, and the dipole field is much smaller. The hyperfine field shows a non-monotonic dependence on the applied Hubbard U_{eff} and the resulting magnetic moment, but never drops below ≈ 1 T. The calculations with a vacancy did not generate a new stopping site, and the calculated hyperfine field was similar to that for a pristine crystal. That is to say, when the calculations are artificially nudged into a magnetic solution by using a

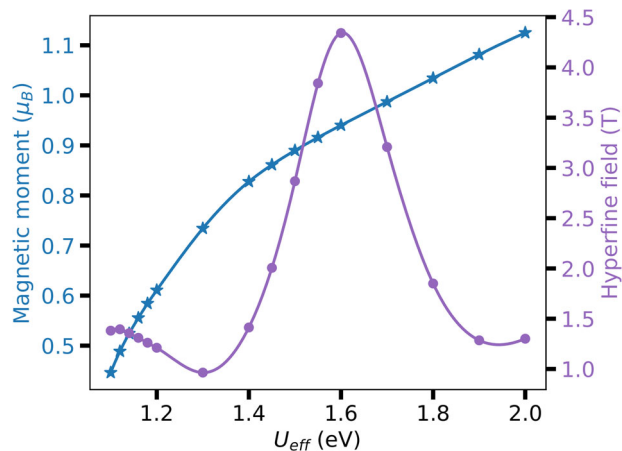


Fig. 11 | Hyperfine field and magnetic moment on Ru as a function of Hubbard U_{eff} . The Fermi-contact term provides the dominant contribution to the hyperfine field, being the dipole field contribution negligible. For U_{eff} values smaller than the plotted ones, the Ru atoms have no magnetic moment. The lines are guides to the eye.

large U_{eff} , the resulting Fermi-contact hyperfine field is a few orders of magnitude stronger than admissible by the experimental constraints. Therefore, we conclude that the nonmagnetic calculations without U (as typical for 4d metals) describe our samples better. Note that in the latter case (and in fact for any $U_{eff} \lesssim 0.6$ eV) the calculations converge to a fully nonmagnetic state, where not only the net magnetic moment around Ru is zero, but also the local spin density is zero everywhere.

Given the large Fermi-contact hyperfine field, we can confidently exclude the presence of anti(alter-)magnetic order. However, even if we exclude metallic electrons at the Fermi level from consideration, the dipole field induced by magnetic moments on Ru already allows us to exclude any static magnetic order. Indeed, the knowledge of the muon stopping site can be used to estimate the relationship between the muon relaxation rate λ_μ and the magnitude of magnetic moments m in RuO_2 . Due to the small magnitude of λ_μ and exponential relaxation of the asymmetry, we assume a dilute arrangement of randomly oriented static moments in our model. Even if the large Fermi-contact field was averaged out, these random moments (located on Ru sites or on magnetic impurities) would still produce a dipolar magnetic field distribution that leads to a relaxation/damping of the polarization of implanted muons.

Considering the exponential relaxation observed experimentally, we assume that the muons in RuO_2 experience a distribution of static magnetic fields $f(|B|)$ that can be described by a Lorentzian function,

$$f(|B|) = \frac{1}{\pi^2} \frac{\Lambda}{(\Lambda^2 + B^2)^2} 4\pi B^2, \quad (2)$$

where Λ is the half-width at half-maximum. In a physical context, Λ can be regarded as the magnitude of the local field B_{loc} , which can be written in terms of the relaxation rate λ_μ in ZF,

$$B_{loc} \approx \Lambda \approx \frac{3\lambda_\mu}{4\gamma_\mu}, \quad (3)$$

where $\gamma_\mu = 851.615$ MHz/T is the muon's gyromagnetic ratio. Therefore, we can put an upper limit on the local static field experienced by muons of 1.3×10^{-5} T in the bulk ($\lambda_\mu \sim 0.015 \mu\text{s}^{-1}$) and 7.0×10^{-5} T in the films ($\lambda_\mu \sim 0.08 \mu\text{s}^{-1}$). Assuming that these fields stem from a dipolar interaction between the muon and a neighboring Ru atom, they can be translated into upper limits of the magnetic moment of $1.14 \times 10^{-4} \mu_B$ in bulk and $7.5 \times 10^{-4} \mu_B$ in films.

Methods

Neutron diffraction

For single crystal neutron diffraction, we employed the large pixelated detector array of the state-of-the-art time of flight diffractometer WISH located at the second target station of the ISIS Neutron and Muon Source of the STFC Rutherford Appleton Laboratory (UK)³⁸. Measurements were performed at 1.5 K using an Oxford Instruments cryostat on four RuO_2 crystals, three of them identified as multi grain, one of them identified as essentially single grain. All measurements led to consistent conclusions. The crystals were aligned in the $(h, 0, l)$ horizontal scattering plane, a large portion of which can be measured in a single shot using the time-of-flight dimension, with the possibility to rotate the crystals about the vertical b^* direction. The normalization of the time of flight diffraction data was performed using the reduction routines implemented in the Mantid software³⁹.

Muon spin relaxation/rotation (μSR)

The μSR experiments on the powder and single crystalline samples were conducted at the General Purpose Surface-Muon (GPS) Instrument⁴⁰ at the Swiss Muon Source piM3.2 beamline of the Paul Scherrer Institute (PSI). A ^4He continuous-flow cryostat was used to perform μSR measurements between 5 K and 290 K. The thin films were studied in the Low-Energy Muons Facility (LEM) at the μE4 beamline at PSI^{41,42}. For these measurements, the thin-film samples were glued onto the cold finger of a ^4He flow cryostat using silver paint. The data analysis for all the μSR spectra was conducted using the *muSRfit* package⁴³.

DFT calculations

DFT calculations were performed with the projector augmented-wave (PAW) method^{44,45}, as implemented in VASP⁴⁶⁻⁵¹. As exchange-correlation functional, we employed the generalized gradient approximation (GGA)⁵² and added an effective Hubbard $U_{eff} = U - J = 1.4$ eV using the rotational invariant GGA+ U introduced in refs. 53 to ensure a sizable magnetic moment on the Ru atoms²² and a non-zero hyperfine field. The cutoff energy for the plane-wave basis was set to 300 eV. We confirmed that, as found in refs. 23,25, the introduction of SOC is negligible. Therefore the calculations were performed without it to optimize computing time. A supercell of $3 \times 3 \times 3$ was used for the mu+DFT calculations, with a KMESH of $2 \times 2 \times 4$ centered around gamma. In order to treat the hydrogen as a proton in VASP, we used the NELECT flag to remove the extra electron. Moreover, this proton was placed not along a high-symmetry line to ensure that the proton ended at the lowest energy position in that plane. To obtain the hyperfine field values, the flag LHYPERFINE was used.

Data availability

The datasets used and/or analysed during the current study are available from the corresponding author on reasonable request.

Received: 17 May 2024; Accepted: 9 August 2024;

Published online: 05 October 2024

References

- Mazin, I. Editorial: Altermagnetism - a new punch line of fundamental magnetism. *Phys. Rev. X* **12**, 040002 (2022).
- Šmejkal, L., Sinova, J. & Jungwirth, T. Emerging research landscape of altermagnetism. *Phys. Rev. X* **12**, 040501 (2022).
- Cuono, G., Sattigeri, R. M., Skolimowski, J. & Autieri, C. Orbital-selective altermagnetism and correlation-enhanced spin-splitting in strongly-correlated transition metal oxides. *J. Magn. Magn. Mater.* **586**, 171163 (2023).
- Šmejkal, L., González-Hernández, R., Jungwirth, T. & Sinova, J. Crystal time-reversal symmetry breaking and spontaneous Hall effect in collinear antiferromagnets. *Sci. Adv.* **6**, eaaz8809 (2020).
- Samanta, K. et al. Crystal Hall and crystal magneto-optical effect in thin films of SrRuO₃. *J. Appl. Phys.* **127**, 21 (2020).
- Feng, Z. et al. An anomalous Hall effect in altermagnetic ruthenium dioxide. *Nat. Electron.* **5**, 735–743 (2022).

7. Gonzalez Betancourt, R. D. et al. Spontaneous anomalous Hall effect arising from an unconventional compensated magnetic phase in a semiconductor. *Phys. Rev. Lett.* **130**, 036702 (2023).
8. Tschimer, T. et al. Saturation of the anomalous Hall effect at high magnetic fields in altermagnetic RuO₂. *APL Mater.* **11**, 2309.00568 (2023).
9. Liu, Q. et al. Inverse magnetocaloric effect in altermagnetic 2D non-van der Waals FeX (X = S and Se) semiconductors. *Adv. Funct. Mater.* **2402080**, 1–10 (2024).
10. Reimers, S. et al. Direct observation of altermagnetic band splitting in CrSb thin films. *Nat. Commun.* **15**, 2116 (2024).
11. Zhou, X. et al. Crystal thermal transport in altermagnetic RuO₂. *Phys. Rev. Lett.* **132**, 056701 (2024).
12. Hariki, A. et al. X-ray magnetic circular dichroism in altermagnetic α -MnTe. *Phys. Rev. Lett.* **132**, 176701 (2024).
13. Guo, Y. et al. Direct and inverse spin splitting effects in altermagnetic RuO₂. *Adv. Sci.* **2400967**, 1–9 (2024).
14. Occhialini, C. A. et al. Local electronic structure of rutile RuO₂. *Phys. Rev. Res.* **3**, 033214 (2021).
15. Liang, Q., Bieberle-Hütter, A. & Brocks, G. Anti-ferromagnetic RuO₂: a stable and robust OER catalyst over a large range of surface terminations. *J. Phys. Chem. C.* **126**, 1337–1345 (2022).
16. Karube, S. et al. Observation of spin-splitter torque in collinear antiferromagnetic RuO₂. *Phys. Rev. Lett.* **129**, 137201 (2022).
17. Fedchenko, O. et al. Observation of time-reversal symmetry breaking in the band structure of altermagnetic RuO₂. *Sci. Adv.* **10**, eadj4883 (2024).
18. Hiraishi, M. et al. Nonmagnetic ground state in RuO₂ revealed by muon spin rotation. *Phys. Rev. Lett.* **132**, 166702 (2024).
19. Prateek, K. et al. Fabrication and properties of lateral Josephson junctions with a RuO₂ weak link. *Superconduct. Sci. Technol.* **37**, 035020 (2024).
20. Zhu, Z. H. et al. Anomalous antiferromagnetism in metallic RuO₂ determined by resonant x-ray scattering. *Phys. Rev. Lett.* **122**, 017202 (2019).
21. Berlijn, T. et al. Itinerant antiferromagnetism in RuO₂. *Phys. Rev. Lett.* **118**, 077201 (2017).
22. Smolyanyuk, A., Mazin, I. I., Garcia-Gassull, L. & Valentí, R. Fragility of the magnetic order in the prototypical altermagnet RuO₂. *Phys. Rev. B* **109**, 134424 (2024).
23. Ahn, K.-H., Hariki, A., Lee, K.-W. & Kuneš, J. Antiferromagnetism in RuO₂ as d-wave Pomeranchuk instability. *Phys. Rev. B* **99**, 184432 (2019).
24. Schäfer, H., Schneiderei, G. & Gerhardt, W. Zur Chemie der Platinmetalle. RuO₂ chemischer Transport, Eigenschaften, thermischer Zerfall. *Z. f. anorganische und allg. Chem.* **319**, 327–336 (1963).
25. Jovic, V. et al. Dirac nodal lines and flat-band surface state in the functional oxide RuO₂. *Phys. Rev. B* **98**, 24 (2018).
26. Keßler, P. et al. Epitaxial RuO₂ and IrO₂ films by pulsed laser deposition on TiO₂(110) **2**, 1–15. <http://arxiv.org/abs/2405.12878> (2024).
27. Lovesey, S. W., Khalyavin, D. D. & van der Laan, G. Magnetic structure of RuO₂ in view of altermagnetism. *Phys. Rev. B* **108**, L121103 (2023).
28. Renninger, M. Umweganregung, eine bisher unbeachtete Wechselwirkungserscheinung bei Raumgitterinterferenzen. *Z. f. Phys.* **106**, 141–176 (1937).
29. Speakman, J. C. The Renninger effect - an example and its implication. *Acta Crystallogr.* **18**, 570–571 (1965).
30. Giacovazzo, C. et al. *Fundamentals of crystallography* (Oxford University Press, 2011).
31. Sazonov, A. et al. Origin of forbidden reflections in multiferroic Ba₂CoGe₂O₇ by neutron diffraction: symmetry lowering or Renninger effect? *J. Appl. Crystallogr.* **49**, 556–560 (2016).
32. Suter, A., Martins, M. M., Ni, X., Prokscha, T. & Salman, Z. Low energy measurements in low-energy μ SR. *J. Phys.: Conf. Ser.* **2462**, 012011 (2023).
33. Esquinazi, P. D. et al. Defect-induced magnetism in nonmagnetic oxides: basic principles, experimental evidence, and possible devices with ZnO and TiO₂. *Physica Status Solidi (b)* **257**, (2020).
34. Blundell, S., De Renzi, R., Lancaster, T. & Pratt, F. L. *Muon spectroscopy: an introduction* (Oxford University Press, 2022).
35. Blundell, S. J. Spin-polarized muons in condensed matter physics. *Contemp. Phys.* **40**, 175–192 (1999).
36. Adamantopoulos, T. et al. Spin and orbital magnetism by light in rutile altermagnets (2024).
37. Diulus, J. T., Tobler, B., Osterwalder, J. & Novotny, Z. Thermal oxidation of Ru(0001) to RuO₂ (110) studied with ambient pressure X-ray photoelectron spectroscopy. *J. Phys. D: Appl. Phys.* **54**, 244001 (2021).
38. Chapon, L. C. et al. Wish: The new powder and single crystal magnetic diffractometer on the second target station. *Neutron News*, 22, 22–25 (2011).
39. Arnold, O. et al. Mantid—Data analysis and visualization package for neutron scattering and μ SR experiments. *Nucl. Instrum. Methods Phys. Res. Sect. A: Accelerators, Spectrometers, Detect. Associated Equip.* **764**, 156–166 (2014).
40. Amato, A. et al. The new versatile general purpose surface-muon instrument (GPS) based on silicon photomultipliers for μ SR measurements on a continuous-wave beam. *Rev. Sci. Instrum.* **88**, 093301 (2017).
41. Morenzoni, E. et al. Generation of very slow polarized positive muons. *Phys. Rev. Lett.* **72**, 2793 (1994).
42. Prokscha, T. et al. The New μ E4 Beam at PSI: a hybrid-type large acceptance channel for the generation of a high intensity surface-muon beam. *Nucl. Instrum. Methods Phys. Res. Sect. A* **595**, 317–331 (2008).
43. Suter, A. & Wojek, B. Musffit: a free platform-independent framework for μ SR data analysis. *Phys. Procedia* **30**, 69–73 (2012).
44. Kresse, G. & Joubert, D. From ultrasoft pseudopotentials to the projector augmented-wave method. *Phys. Rev. B* **59**, 1758 (1999).
45. Blöchl, P. E. Projector augmented-wave method. *Phys. Rev. B* **50**, 17953 (1994).
46. Kresse, G. & Hafner, J. Ab initio molecular dynamics for liquid metals. *Phys. Rev. B* **47**, 558–561 (1993).
47. Kresse, G. & Hafner, J. Ab initio molecular-dynamics simulation of the liquid-metal-amorphous-semiconductor transition in germanium. *Phys. Rev. B* **49**, 14251–14269 (1994).
48. Kresse, G. & Furthmüller, J. Efficiency of ab-initio total energy calculations for metals and semiconductors using a plane-wave basis set. *Comput. Mater. Sci.* **6**, 15–50 (1996).
49. Kresse, G. & Furthmüller, J. Efficient iterative schemes for ab initio total-energy calculations using a plane-wave basis set. *Phys. Rev. B* **54**, 11169–11186 (1996).
50. Perdew, J. P., Burke, K. & Ernzerhof, M. Generalized gradient approximation made simple. *Phys. Rev. Lett.* **77**, 3865–3868 (1996).
51. Perdew, J. P., Burke, K. & Ernzerhof, M. Generalized gradient approximation made simple [Phys. Rev. Lett. 77, 3865 (1996)]. *Phys. Rev. Lett.* **78**, 1396–1396 (1997).
52. Ernzerhof, M., Burke, K. & Perdew, J. P. Density functional theory, the exchange hole, and the molecular bond. *Theor. Comput. Chem.* **4**, 207–238 (1996).
53. Liechtenstein, A. I., Anisimov, V. I. & Zaanen, J. Density-functional theory and strong interactions: Orbital ordering in Mott-Hubbard insulators. *Phys. Rev. B* **52**, R5467 (1995).
54. Momma, K. & Izumi, F. VESTA3 for three-dimensional visualization of crystal, volumetric and morphology data. *J. Appl. Crystallogr.* **44**, 1272–1276 (2011).
55. Kim, H.-D., Noh, H.-J., Kim, K. H. & Oh, S.-J. Core-level X-ray photoemission satellites in ruthenates: a new mechanism revealing the Mott transition. *Phys. Rev. Lett.* **93**, 126404 (2004).

Acknowledgements

We thank Helena Reichlova, Dominik Kriegner, Libor Smejkal, Thomas Jungwirth and Huibo Cao for helpful discussions. We further gratefully acknowledge Martin Klement and Charles Gould for their support in the SQUID measurements. Funding support came from the Deutsche Forschungsgemeinschaft (DFG, German Research Foundation) under Germany's Excellence Strategy through the Würzburg-Dresden Cluster of Excellence on Complexity and Topology in Quantum Matter ct.qmat (EXC 2147, Project ID 390858490) and through the Collaborative Research Center SFB 1170 ToCoTronics (Project ID 258499086). L.G.G. and R.V. further gratefully acknowledge support by the Deutsche Forschungsgemeinschaft (DFG, German Research Foundation) for funding through project TRR 288 — 422213477 (project B05). I.I.M. was supported by the Army Research Office under Cooperative Agreement Number W911NF-22-2-0173. He also acknowledges Heraeus Foundation for supporting his visits to the University of Frankfurt. This work is partially based on experiments performed at the Swiss Muon Source ($S\mu S$), Paul Scherrer Institute, Villigen, Switzerland. Some of the images in the paper were created using VESTA software⁵⁴. The supplementary information contains additional ref. 55.

Author contributions

P.K. and L.G.G. contributed equally. I.I.M., R.V., S.M. conceived the project. P.K. and S.M. synthesized and characterized the RuO_2 thin films. D.K., P.M. and F.O. performed the neutron scattering experiments and analysis. P.K., S.M., Z.S., A.S. and T.P. performed the μSR experiments and analysis and L.G.G. and I.I.M. performed the DFT+U+ μ calculations. All authors contributed to the discussions and the writing of the paper.

Funding

Open Access funding enabled and organized by Projekt DEAL.

Competing interests

The authors declare no competing interests.

Additional information

Supplementary information The online version contains supplementary material available at <https://doi.org/10.1038/s44306-024-00055-y>.

Correspondence and requests for materials should be addressed to Zaher Salman, Pascal Manuel, Igor I. Mazin, Roser Valentí or Simon Moser.

Reprints and permissions information is available at <http://www.nature.com/reprints>

Publisher's note Springer Nature remains neutral with regard to jurisdictional claims in published maps and institutional affiliations.

Open Access This article is licensed under a Creative Commons Attribution 4.0 International License, which permits use, sharing, adaptation, distribution and reproduction in any medium or format, as long as you give appropriate credit to the original author(s) and the source, provide a link to the Creative Commons licence, and indicate if changes were made. The images or other third party material in this article are included in the article's Creative Commons licence, unless indicated otherwise in a credit line to the material. If material is not included in the article's Creative Commons licence and your intended use is not permitted by statutory regulation or exceeds the permitted use, you will need to obtain permission directly from the copyright holder. To view a copy of this licence, visit <http://creativecommons.org/licenses/by/4.0/>.

© The Author(s) 2024

Absence of magnetic order in RuO₂: insights from μ SR spectroscopy and neutron diffraction – Supplementary Information –

Philipp Keßler,^{1,2} Laura Garcia-Gassull,³ Andreas Suter,⁴ Thomas Prokscha,⁴ Zaher Salman,⁴ Dmitry Khalyavin,⁵ Pascal Manuel,⁵ Fabio Orlandi,⁵ Igor I. Mazin,⁶ Roser Valentí,³ and Simon Moser^{1,2}

¹Physikalisches Institut, Universität Würzburg, 97074 Würzburg, Germany

²Würzburg-Dresden Cluster of Excellence ct.qmat, Universität Würzburg, 97074 Würzburg, Germany

³Institut für Theoretische Physik, Goethe-Universität, 60438 Frankfurt am Main, Germany

⁴Laboratory for Muon Spin Spectroscopy, Paul Scherrer Institute, CH-5232 Villigen PSI, Switzerland

⁵ISIS Pulsed Neutron and Muon Source, STFC Rutherford Appleton Laboratory, Didcot, OX11 0QX, United Kingdom

⁶George Mason University, Department of Physics & Astronomy and Quantum Science and Engineering Center, Fairfax, USA

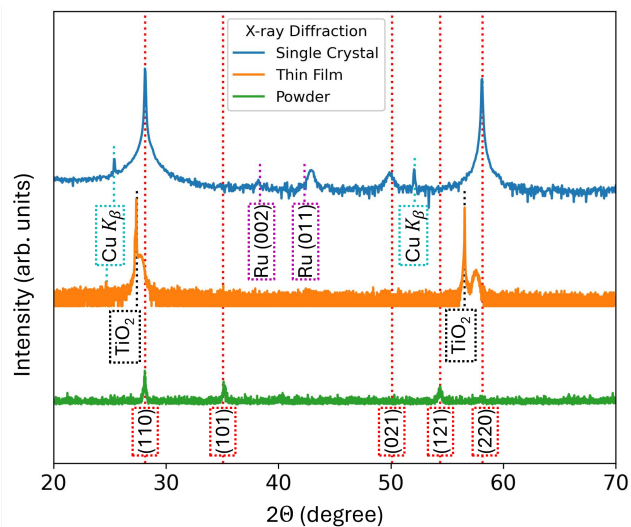
(Dated: July 5, 2024)

Sample characterization

Supplementary Fig. S1 shows X-ray diffraction (XRD) survey scans of our RuO₂ single crystal, thin films and powder, measured with Cu K α (8.05 keV) radiation. For better visibility of the line-shape of the individual Bragg peaks, the data of the single crystal and the thin film is depicted on a log scale, while the powder data is depicted on a linear scale. In all samples, we clearly identify the structural (110) and (220) Bragg peaks of RuO₂. In the single crystal, we additionally observe the (021) Bragg peak of a differently oriented RuO₂ crystallite, as well as signatures of crystalline Ru inclusions. The thin film additionally exhibits the sharp (110) and (220) Bragg reflections of the TiO₂ substrate. Using the RuO₂ and TiO₂ bulk lattice constants as reference, we find that the lattice constant of the RuO₂ thin film is about 1.0% larger than its bulk counterpart due to epitaxial strain [1]. The RuO₂ powder further exhibits the structural (101) and (121) peaks. Finally, we find artificial signatures of the RuO₂ (110) and (220) as well as TiO₂ (110) Bragg reflections in single crystal and thin film resulting from residual Cu K β radiation from the x-ray source.

Supplementary Fig. S2 shows representative X-ray photoelectron spectroscopy (XPS) measurements of our RuO₂ single crystal, thin film and powder, using a monochromatic Al K α X-ray source with 1486.7 eV radiation. Panel (a) shows a survey scan, demonstrating the chemical purity of the thin film and powder surfaces within the sensitivity of the experiment. Panel (b) shows a detailed scan of the Ru 3d multiplet, confirming the RuO₂ stoichiometry of all three samples [2]. In contrast to film and powder, the single crystal surface exhibits three types of impurities: (i) a tellurium contamination resulting from residues of the TeCl₄ transport agent used in the chemical vapor transport growth process [3]; (ii) a carbon contamination that overlaps with the screened Ru 3d 3/2 spectral weight [2] and results from organic solvents; and (iii) a very slight chromium contamination – possibly resulting from handling the crystal with chromium-plated tweezers in the past.

As the overall volume of the film is low and the single crystal subject to slight magnetic impurities, the dependence of

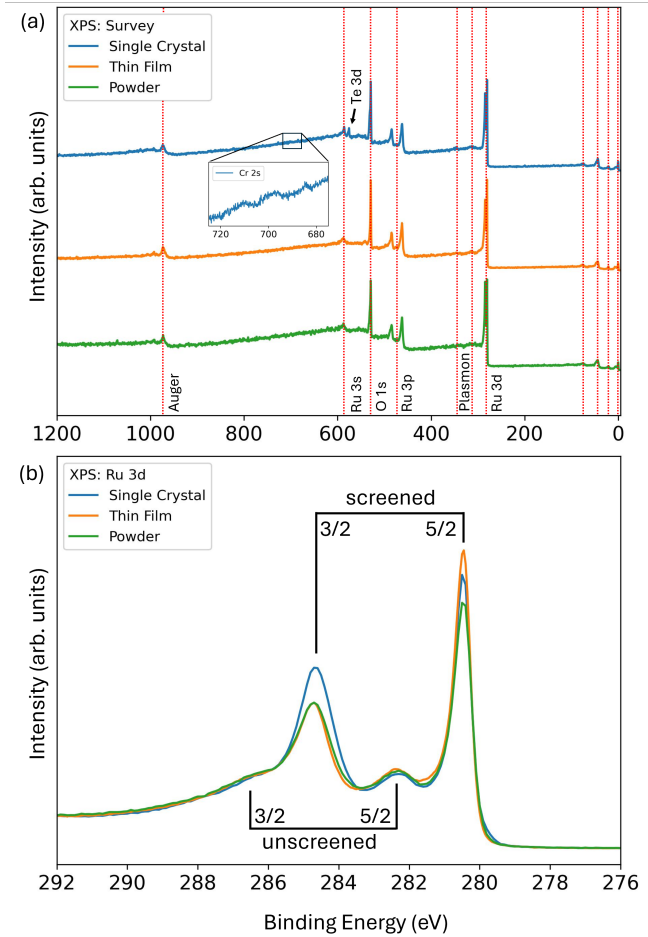


Supplementary Figure S1. The X-ray diffraction (XRD) survey scans indicate a well defined crystal structure of the respective samples. For a better readability, the single crystal and thin film data are depicted in logarithmic- and the powder data in linear scale.

the total magnetization of pure RuO₂ on external magnetic fields is best reflected in the RuO₂ powder. Corresponding superconducting quantum interference device (SQUID) magnetometry measurements at $T = 10$ K are shown in supplementary Fig. S3, and clearly exhibit the linear slope expected from a paramagnet.

Supplementary calculations

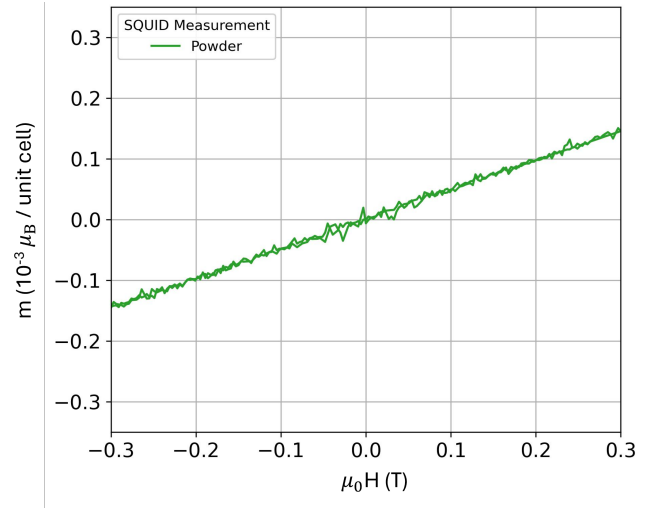
RuO₂ crystallizes in the rutile crystal structure, space group P4₂/mnm. The unit cell of the crystal is shown in the left of supplementary Fig. S4, such that the unit cell is formed by two Ru atoms, to account for the spin polarized component, and four oxygen atoms. The octahedra formed by the oxygens around the Ru atoms are shown in light gray color, exposing the four-fold rotation from one Ru sublattice to the other. We used this structure to study the



Supplementary Figure S2. (a) X-ray photoelectron spectroscopy (XPS) survey scans of the RuO_2 samples used in this study. The tellurium (Te) detected on the single crystal results from the transport agent TeCl_4 , that was used during sample growth. Peaks measured for binding energies below 100 eV are: Ru 4s, Ru 4p, O 2s and Ru 4d. (b) An XPS detail scan of the Ru 3d multiplet highlights a similar chemical composition of all three samples. The apparent increase in Ru 3d 3/2 spectral weight for the RuO_2 single crystal points towards a slight carbon contamination and thus an augmented C 1s signature.

behavior of the local potential in the pristine case. The relaxed lattice parameters used are $a = b = 4.533132 \text{ \AA}$ and $c = 3.124167 \text{ \AA}$.

The middle and right panels of supplementary Fig. S4 show different perspectives of an isosurface of the electrostatic potential within the unit cell. The top view of the middle panel shows the maxima of the potential to occur in between the Ru rows, outside of the octahedra shown in the left panel. Moreover, there is a slight tilt in the isosurface due to the coordination of the nearby oxygens. The right panel shows the tube-like shape of the isosurface along the crystal c -axis, as well as the supercell used in the calculations. The

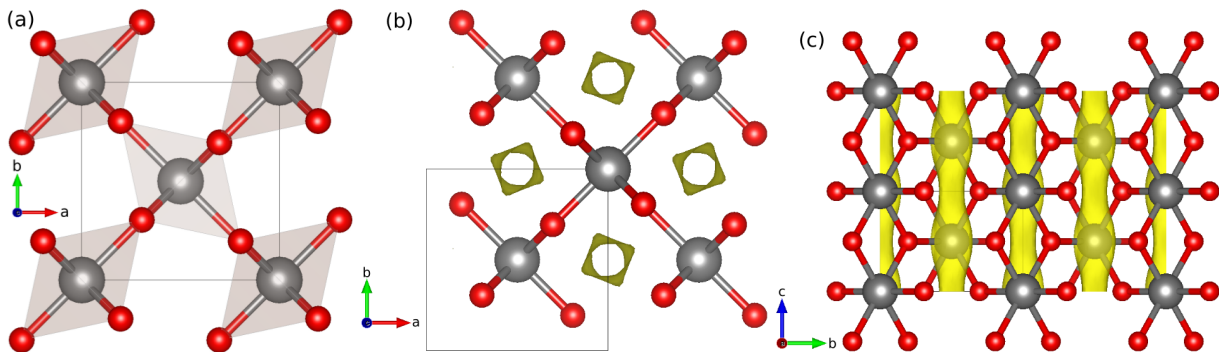


Supplementary Figure S3. SQUID measurement at $T = 10 \text{ K}$ of the powder sample showing a paramagnetic behavior.

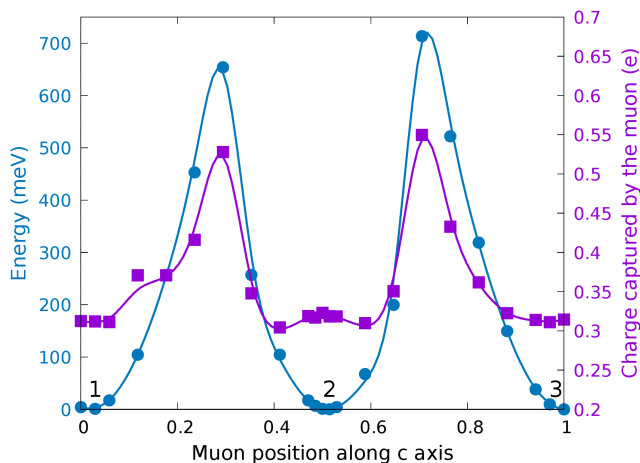
muon decays somewhere along this tube. The reason to use a supercell is such that the interaction between a muon and its replica in the neighbouring cell is negligible [4].

Supplementary Fig. S5 shows the energy of the system, compared to the ground state energy, as well as the charge captured by the muon for different positions along the z axis, in fractionalized coordinates. The minima of the energy occur when closest to the oxygens. Multiple calculations were performed in order to avoid finding a local minimum of the potential energy surface. On the other hand, the muon capturing charge from the environment is a possible occurrence [4]. The evolution of the charge captured by the muon shows that, when it is closest to the oxygens (see Fig. 9 in the main text), the electron screening is higher and hence there is a lower charge captured by the muon.

Supplementary Fig. S6 shows a supercell of $3 \times 3 \times 3$ with one Ru vacancy, represented in white centered in the unit cell. This vacancy accounts for $\approx 2\%$ of vacancies, as reported in Ref. [5]. A color map is used to represent the electrostatic potential, with the previously seen absolute maxima in between the octahedra. Moreover, the new electrostatic potential due to the Ru vacancy is shown. Note the breaking of C_4 symmetry from the oxygens that would have been bonded to the missing Ru. Those oxygens are the ones with the largest displacement, 0.0953 \AA , towards the vacancy. Furthermore, around the vacancy, the electrostatic potential indicates a possible new stopping site. Hence, a muon was placed nearby the vacancy, more specifically in the (001) plane with the vacancy, to study the energy of the system and compare it to the previously found stopping sites to determine if it was likely the muon ended there. The muon was placed in this plane given the knowledge of its preference to bond with the oxygen and the previously minima energy found in the pristine case. Note that the final



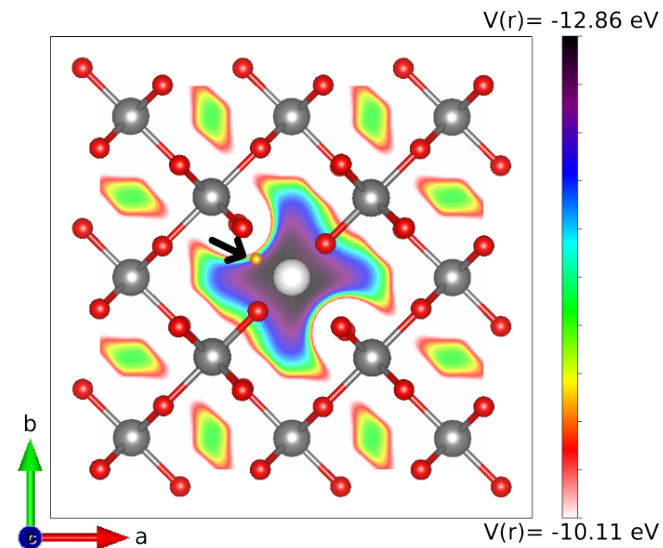
Supplementary Figure S4. (a): Crystal structure of RuO_2 : Ru atoms are represented in gray while O atoms are in red. The projection on the ab plane of the rotated RuO_6 octahedra is shown in shaded gray (note a 90° rotation of the octahedra around two sublattice Ru). The square shows the unit cell used in calculations without a muon. (b): Top view of the isosurface of the Coulomb potential with value -11.2 eV calculated with $U_{eff} = 1.4$ eV, indicating the initial approximation for muon stopping sites. (c): Same, a side view.



Supplementary Figure S5. Energy of the system (in meV) -left axis- and charge captured by the muon (in electron units) -right axis- for different positions of the muon along the c direction (the positions are given in fractionalized units of the c lattice parameter). The charge the muon is captured from the bond it creates with the nearest O atom, as shown in Fig. 9 of the main text. The closer to the oxygen atom the muon is, the more screening the muon has and therefore the captured charge is lower, which occurs when the energy of the system is the lowest as well.

stopping site of the muon was not at the absolute maxima of the electrostatic potential, due to this tendency to bond with an O atom. However, no new possible stopping sites that were energetically favorable were found. Therefore, the

distance between the most likely stopping sites of the muon found in Fig. 9 of the main text and the closest Ru atom was used to analyze the data of the μSR experiments.



Supplementary Figure S6. Top view of a color map of the electrostatic potential of a pristine crystal with a Ru vacancy. Here, the U_{eff} is 1.4 eV. A muon, represented in orange, was placed nearby the Ru vacancy, shown in white, to check for possible new stopping sites. The arrow points to the muon, which is shown in the final stopping site, where it sits near an O atom and creates a bond with it.

[1] Keßler, P. *et al.* Epitaxial RuO_2 and IrO_2 films by pulsed laser deposition on TiO_2 (110) **2**, 1–15 (2024). URL <http://arxiv.org/abs/2405.12878>. arXiv:2405.12878.

[2] Kim, H.-D., Noh, H.-J., Kim, K. H. & Oh, S.-J. Core-Level X-Ray Photoemission Satellites in Ruthenates: A New Mechanism Revealing The Mott Transition. *Physical Review Let-*

- ters **93**, 126404 (2004). URL <https://link.aps.org/doi/10.1103/PhysRevLett.93.126404>. 0403066.
- [3] Jovic, V. *et al.* Dirac nodal lines and flat-band surface state in the functional oxide RuO₂. *Physical Review B* **98**, 24 (2018). URL <https://link.aps.org/doi/10.1103/PhysRevB.98.241101>.
- [4] Blundell, S., De Renzi, R., Lancaster, T. & Pratt, F. L. *Muon Spectroscopy: An Introduction* (Oxford University Press, 2022).
- [5] Diulus, J. T., Tobler, B., Osterwalder, J. & Novotny, Z. Thermal oxidation of Ru(0001) to RuO₂ (110) studied with ambient pressure x-ray photoelectron spectroscopy. *Journal of Physics D: Applied Physics* **54**, 244001 (2021). URL <https://iopscience.iop.org/article/10.1088/1361-6463/abcd>.